

# Water-Promoted C–C Coupling Reaction in Plasma-Catalytic CO<sub>2</sub> Hydrogenation for Ethanol Production

Shengyan Meng,<sup>▽</sup> Zhaolun Cui,<sup>▽</sup> Qian Chen,<sup>▽</sup> Hang Zhang, Shangkun Li, Erik Cornelis Neyts, Evgenii Vlasov, Kellie Jenkinson, Sara Bals, Dezheng Yang, Min Liu,\* Yi Liu,\* Annemie Bogaerts, An-Hui Lu,\* and Yanhui Yi\*



Cite This: *ACS Catal.* 2025, 15, 3236–3246



Read Online

ACCESS |



Metrics & More



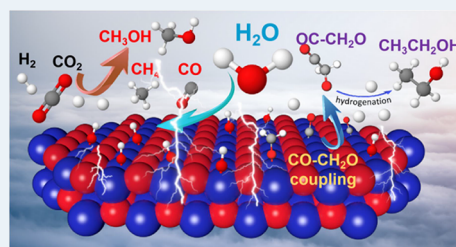
Article Recommendations



Supporting Information

**ABSTRACT:** The conversion of CO<sub>2</sub> into alcohols has attracted widespread interest. Herein, we present an approach for the plasma-catalytic CO<sub>2</sub> hydrogenation to ethanol over a Cu<sub>2</sub>O/CeO<sub>2</sub> catalyst under atmospheric pressure at a low temperature of ~75 °C. The Cu<sub>2</sub>O/CeO<sub>2</sub> catalyst initially exhibits low ethanol selectivity (2.1%), which dramatically increases to 56% (78% total alcohols selectivity) with the assistance of water. D<sub>2</sub>O and H<sub>2</sub><sup>18</sup>O isotope-tracing experiments reveal the partial decomposition of water and the active involvement of its derivatives in the multistep pathway for ethanol synthesis. The multiple roles of H<sub>2</sub>O in switching alcohols production from methanol to ethanol are investigated. The plasma-generated OH in both adsorbed and radical states promotes C–C coupling via CO–H<sub>2</sub>CO bonding and facilitates hydrogenation through proton transfer. Additionally, the presence of adsorbed H<sub>2</sub>O and OH enhances the desorption of ethanol, further enhancing alcohol selectivity. It is envisaged that these findings would inspire value-added transformation of CO<sub>2</sub> to produce higher alcohols and pave the way for efficient chemical processes.

**KEYWORDS:** CO<sub>2</sub> hydrogenation, plasma catalysis, C<sub>2</sub>H<sub>5</sub>OH synthesis, C–C coupling, water-assisted catalysis, copper-based catalysts, DFT calculations



## 1. INTRODUCTION

As a major greenhouse gas, carbon dioxide (CO<sub>2</sub>) holds the potential to serve as an abundant, cheap, and renewable carbon source. Carbon capture and utilization (CCU) technology plays a pivotal role in converting CO<sub>2</sub> into high-value-added chemicals, thereby contributing to the development of a sustainable low-carbon economy.<sup>1</sup> At present, significant advancements have been achieved in the conversion of CO<sub>2</sub> to carbon monoxide (CO), alcohols, olefins, and aromatics.<sup>2–6</sup> Among the alcohols products, ethanol (C<sub>2</sub>H<sub>5</sub>OH) has a higher energy density than methanol (CH<sub>3</sub>OH) and has been widely used as a disinfectant, solvent, and renewable fuel additive.<sup>7</sup>

However, the hydrogenation of CO<sub>2</sub> to C<sub>2</sub>H<sub>5</sub>OH remains a formidable challenge due to the thermodynamic stability of CO<sub>2</sub> and the intricacies involved in controlling C–C coupling reactions. Initially, Rh-based catalyst, as pioneered by Tanabe's group, demonstrated promise in this direction.<sup>8</sup> Besides the typical Rh-based catalysts, other noble metal catalysts (Au,<sup>9</sup> Pt,<sup>10</sup> Pd-based<sup>11</sup>) have been explored for CO<sub>2</sub> hydrogenation to C<sub>2</sub>H<sub>5</sub>OH. In recent years, non-noble metal and transition metal carbide catalysts have garnered significant attention as alternatives for CO<sub>2</sub> hydrogenation to C<sub>2</sub>H<sub>5</sub>OH, in which Cu- and Co-based catalysts have been shown effective on C<sub>2</sub>H<sub>5</sub>OH yields in thermal catalysis.<sup>12–16</sup> Nevertheless, as summarized in Table S1, most reported catalysts evaluated in fixed-bed reactors have struggled with poor C<sub>2</sub>H<sub>5</sub>OH selectivity.

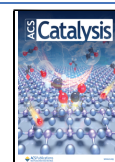
In thermal catalysis, CO<sub>2</sub> hydrogenation for C<sub>2</sub>H<sub>5</sub>OH production can be improved by adding water (H<sub>2</sub>O) to the feedstock. H<sub>2</sub>O and its dissociation products are found to play a paramount role in C–C coupling and the generation of alcohols.<sup>10,17–21</sup> He et al. reported water-promoted higher alcohols (C<sub>2</sub>–C<sub>4</sub>) generation at 200 °C over a Pt/Co<sub>3</sub>O<sub>4</sub> catalyst, achieving an ethanol selectivity of 17.3%.<sup>10</sup> They presumed that water could facilitate the dissociation of CH<sub>3</sub>OH into CH<sub>3</sub>\* (\* means the adsorbed state), leading to C–C coupling through the CO\*–CH<sub>3</sub>\* mechanism. Graciani et al. evaluated the multiple roles of H<sub>2</sub>O on CO<sub>2</sub> conversion to ethanol over a Pt/CeO<sub>x</sub>/TiO<sub>2</sub>(110) catalyst, showing an optimal ethanol selectivity of 38% at 280 °C and 5 bar.<sup>19</sup> Water was found to promote the first hydrogenation step and enhance the surface coverage of C-containing species, which facilitates the C–C bond formation via CH<sub>3</sub>\*–H<sub>2</sub>CO\* coupling. As is clear from these examples, the C<sub>2</sub>H<sub>5</sub>OH synthesis in thermal catalysis often requires relatively high

Received: October 24, 2024

Revised: January 17, 2025

Accepted: January 21, 2025

Published: February 7, 2025



temperatures and pressures, hindering its applications under milder conditions.

In contrast, plasma catalysis is gaining increasing interest as it enables thermodynamically unfavorable reactions to proceed near room temperature and at atmospheric pressure.<sup>22</sup> Especially the nonequilibrium species and discharge effects reduce the activation barriers for rate-limiting steps and break the scaling relations, providing an attractive alternative for CO<sub>2</sub> conversion.<sup>23</sup> Currently, plasma-catalytic CO<sub>2</sub> hydrogenation has been investigated focusing on the production of C1 molecules (CO, CH<sub>4</sub>, and CH<sub>3</sub>OH).<sup>24,25</sup> Plasma-generated reactive species have been demonstrated to play a significant role in guiding the surface catalytic reactions via unique effects, including surface modification, preadsorption, and Eley–Rideal (E-R) reactions.<sup>20,26,27</sup> In this regard, combining with inspiration from He et al. that H<sub>2</sub>O molecules promote C–C coupling reaction for C<sub>2</sub>H<sub>5</sub>OH production,<sup>10</sup> we may speculate that plasma-activated H<sub>2</sub>O could have multiple roles in guiding the CO<sub>2</sub> hydrogenation to C<sub>2</sub>H<sub>5</sub>OH at mild conditions.

Herein, we report a novel plasma catalysis approach, achieving C<sub>2</sub>H<sub>5</sub>OH synthesis from CO<sub>2</sub> hydrogenation over a cost-effective Cu<sub>2</sub>O/CeO<sub>2</sub> catalyst with the assistance of water at atmospheric pressure and ca. 75 °C (Figure S1 provides the temperature distribution measured by an infrared camera), showing ca. 56% C<sub>2</sub>H<sub>5</sub>OH selectivity and a total alcohols (methanol and ethanol) selectivity of around 78%. Furthermore, a combination of isotope-tracing experiments and density functional theory (DFT) calculations reveal the distinct C–C coupling reaction mechanism for C<sub>2</sub>H<sub>5</sub>OH production switched by H<sub>2</sub>O, which is quite different from the mechanism previously reported. In the plasma, the H<sub>2</sub>O molecule is dissociated to produce adsorbed OH\* species and gas-phase OH radicals. The adsorbed OH\* species is identified as a crucial factor in facilitating the C–C coupling reaction and hydrogenation for C<sub>2</sub>H<sub>5</sub>OH formation and its subsequent desorption over the Cu<sup>+</sup> catalyst. The gas-phase OH radicals promote hydrogenation and facilitate OH\* surface coverage. In this regard, the unique roles of water in plasma enable the stable C<sub>2</sub>H<sub>5</sub>OH yield with a high selectivity, which offers new opportunity for higher alcohols production from CO<sub>2</sub>.

## 2. METHODS

**2.1. Catalyst Preparation.** Cu(NO<sub>3</sub>)<sub>2</sub>·5H<sub>2</sub>O (99%) was purchased from Tianjin Guangfu Technology Development Co., Ltd., and oxide-support materials were purchased from Shanghai Buwei Applied Materials Technology Co., Ltd., China. Deionized (DI) water was homemade.

Copper-based catalysts with various supports were prepared via incipient wetness impregnation, utilizing commercially available supports (Al<sub>2</sub>O<sub>3</sub>, SiO<sub>2</sub>, Fe<sub>2</sub>O<sub>3</sub>, CeO<sub>2</sub>, TiO<sub>2</sub>, and ZrO<sub>2</sub>) as supporting materials and subsequently calcined at 540 °C prior to use. Initially, the precursor salt Cu(NO<sub>3</sub>)<sub>2</sub>·5H<sub>2</sub>O was dissolved in DI water, and then the support was added to the solution and stirred for 15 min. A fixed Cu loading of 5 wt % was achieved by adjusting the amount of precursor salt accordingly (XRF results indicate an actual loading of approximately 5.5 wt %). Subsequently, the mixture was aged at room temperature for 12 h and then overnight dried at 120 °C in air. Following this, the samples underwent calcination in the air for 5 h in a muffle furnace at 800 °C and were finally crushed and sieved into granules (20–40 mesh). To investigate the physicochemical properties of the catalysts, both fresh and spent catalysts were characterized by various

methods. The fresh catalyst is denoted as Cat-F, while the collected spent catalyst is denoted as Cat-S ( $x - 1$ ), with  $x$  representing the content of H<sub>2</sub>O based on CO<sub>2</sub>.

**2.2. Catalytic Test.** The schematic diagram of the experimental equipment is shown in Scheme S1. A coaxial dielectric barrier discharge (DBD) reactor with a water electrode was used to generate CO<sub>2</sub>/H<sub>2</sub> plasma. A stainless-steel tube (2 mm outer diameter) was placed in the center of a DBD reactor, consisting of a pair of coaxial quartz cylinders (inner and outer quartz tubes) as high-pressure electrodes. The temperature of the circulating water (grounded electrode) was maintained at 60 °C, the discharge length was 60 mm, and the 4 mm discharge gap was completely packed by catalyst granules (20–40 mesh, ca. 2.2 g of Cu<sub>2</sub>O/CeO<sub>2</sub> catalyst). The input power was maintained at around 23 W, and the discharge frequency was fixed at 9.5 kHz. The individual reaction duration ranged from 3 to 5 h, depending on the addition of water content.

CO<sub>2</sub> (98%, 18 mL/min) and H<sub>2</sub> (99.99%, 54 mL/min) were monitored using mass flow controllers and homogeneously mixed with water vapor generated by a steam generator at 110 °C before being passed through the plasma reactor. The use of heating tape ensured complete encapsulation of the reactor by the gas before contact with the catalyst, thus guaranteeing the vaporized state of water. In this study, the maximum flow rate of gaseous water was 36 mL/min, while the liquid water flow rate at the pump was 28.93 μL/min. It should be mentioned that the plasma discharge is influenced when the H<sub>2</sub>O/CO<sub>2</sub> molar ratio exceeds 2 due to the electronegativity of H<sub>2</sub>O. The liquid product was collected by a collector (mixture of isopropyl alcohol and liquid nitrogen below –120 °C) at the exhaust of the DBD reactor, and the decrease of the gas flow rate was measured by a soap-film flow meter. The distance between the exhaust pipe and the soap bubble flow meter was 3 m, with a 6 mm inner diameter silicone tube, to mitigate the impact of product condensation on the gas velocity. The composition of the exhaust gas was analyzed online by gas chromatography (Tianmei 7890 II equipped with a thermal conductivity detector and a TDX-01 chromatography column with H<sub>2</sub> as the carrier gas). The flame ionization detector used a TM-Al<sub>2</sub>O<sub>3</sub>/S column with N<sub>2</sub> as the carrier gas) with the addition of 2% N<sub>2</sub> as an internal standard. The gas chromatography method samples every 15 min (with the exhaust gases being detected 2 h later), and the final result is determined through the calculation of the average value (totaling approximately eight results). Liquid products were analyzed by gas chromatography (Shimadzu GC-2014C, equipped with a flame ionization detector and a PEG-20 M column) and GC-MS (Agilent 5975C, DB-1701 column). The mass spectrometry (MS) signal intensity of the exhaust gas was measured in situ by a mass spectrometer (PFEIFFER, OmniStar) using the SEM scanning mode. Considering the initial stage of the reaction, partial reduction of the Cu species will cause weak fluctuations in the MS signal, and the sample used for MS analysis is the spent catalyst.

**2.3. Catalyst Characterization.** The crystal structure of the catalyst was determined by using a powder X-ray diffractometer (Rigaku, D-max 2400) with CuK $\alpha$  radiation. The measurement was operated in the range of 10–80° with a scanning rate of 5°/min at 50 mA and 240 kV. The texture information on the samples was measured by N<sub>2</sub> physisorption (Micromeritics ASAP 3020) at –196 °C. Before the measurement, the samples (0.2 g) were degassed at 350 °C

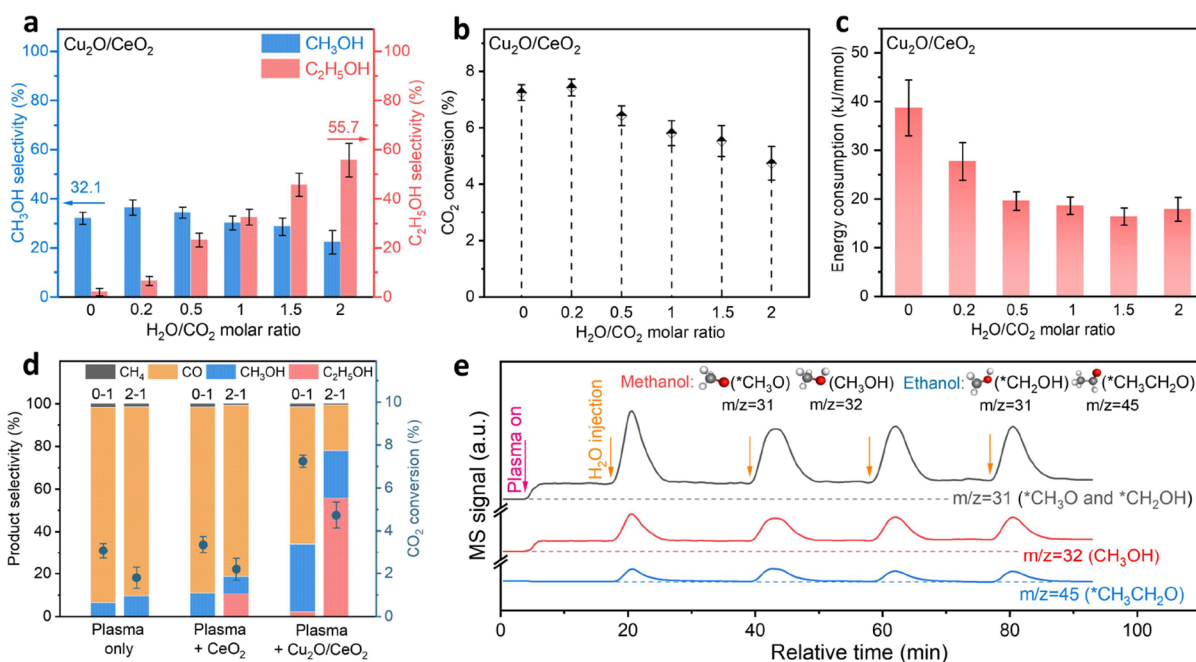


**Figure 1.** (a–c) Influence of  $\text{H}_2\text{O}/\text{CO}_2$  molar ratio on (a) product selectivity, (b)  $\text{CO}_2$  conversion, and (c) energy consumption for  $\text{C}_2\text{H}_5\text{OH}$  and  $\text{CH}_3\text{OH}$  production over a 5 wt %  $\text{Cu}_2\text{O}/\text{CeO}_2$  catalyst (2.2 g). (d) Influence of reaction system and presence/absence of  $\text{H}_2\text{O}$  on product selectivity and  $\text{CO}_2$  conversion (0–1 and 2–1 represent the  $\text{H}_2\text{O}/\text{CO}_2$  molar ratio). (e) Temporal profiles of MS signals with different  $m/z$  values (corresponding to different species) in  $\text{CO}_2$  hydrogenation through plasma catalysis over 5 wt %  $\text{Cu}_2\text{O}/\text{CeO}_2$  catalyst (2.2 g, prerduced catalyst) with intermittent addition of  $\text{H}_2\text{O}$  for 3 min of each injection (molar ratio of  $\text{H}_2\text{O}/\text{CO}_2 = 2/1$ ). (Reaction conditions: 5 wt % Cu loading,  $\text{CO}_2/\text{H}_2 = 1/3$ , input power 23 W, discharge frequency 9.5 kHz,  $75^\circ\text{C}$ , 1 atm pressure; error bars represent the standard deviation from at least three independent measurements).

for 5 h. The surface area was determined based on the Brunauer–Emmett–Teller (BET) method, and the pore volume of the samples was calculated by the t-plot method at a  $P/P_0$  of 0.99. High-angle annular dark-field scanning transmission electron microscopy (HAADF-STEM) images of the catalysts were obtained using a “cubed” Thermo Fisher Scientific X-Ant-EM electron microscope operated at 300 kV. Energy-dispersive X-ray spectroscopy (EDX) mapping was used to retrieve the elemental distribution over the sample surface. The reduction properties of the catalysts were measured on a ChemBET Pulsar (Quanta chrome) chemical adsorption instrument. The samples (0.5 g) were purged for 1 h at  $450^\circ\text{C}$  under a He atmosphere. After being cooled to room temperature, the samples were heated to  $500^\circ\text{C}$  at a rate of  $10^\circ\text{C}/\text{min}$  in an  $\text{Ar}-\text{H}_2$  atmosphere (120 mL/min, 10%  $\text{H}_2$ ), and a TCD was used to detect the hydrogen consumption. X-ray photoelectron spectroscopy (XPS) was carried out on an ESCALAB 250Xi instrument (ThermoVG) with an  $\text{AlK}\alpha$  X-ray source. The binding energy value of C 1s (284.8 eV) was taken as the reference level to obtain chemical information on the elements on the catalyst surface. Ar+ etching was carried out under the conditions of 2 kV by bombarding the catalyst surface. In this study,  $\text{SiO}_2$  was chosen as the standard sample with an etching rate set at approximately 10 nm/min. Hence, 60 s etching time resulted in an etch depth of approximately 10 nm on the catalyst surface. All catalysts were sealed in vacuum bags prior to characterization tests.

**2.4. Plasma Diagnostics.** The electrical behavior was characterized by three indicators: discharge voltage (kV), discharge current (mA), and discharge frequency (kHz), which were detected by a digital oscilloscope (Tektronix, DPO 3012)

with a high voltage probe and a current probe. In plasma systems, the Lissajous plots represent the charge in the plasma as a function of voltage, and the enclosed area denotes the average power consumed by the discharge, i.e., the product of energy consumed per cycle and the frequency of the cycle. Furthermore, we used an in situ Princeton Instruments ICCD emission spectrometer (SP 2758) with a 300 g/mm grating to diagnose the optical behavior in the  $\text{CO}_2/\text{H}_2$  plasma. The slit width of the spectrometer was fixed at  $20\ \mu\text{m}$ , and the exposure time was fixed at 2 s.

**2.5. DFT Calculation.** All DFT calculations were performed in the CP2K 7.0 package with the Quickstep module.<sup>28,29</sup> The molecular optimized and double- $\zeta$  valence plus polarization basis set was chosen combined with an auxiliary plane wave basis set with a 600 Ry cutoff.<sup>30</sup> The Goedecker-Teter-Hutter pseudopotential was applied for core–valence interactions.<sup>31</sup> The exchange and correlation effects were treated by the Perdew–Burke–Ernzerhof functional with spin unrestricted. Dispersion interactions were accounted for using Grimme’s D3 approximation, together with Becke–Johnson damping.<sup>32,33</sup> The sampling of the Brillouin zone was limited to the  $\Gamma$ -point only.<sup>34</sup> The Broyden–Fletcher–Goldfarb–Shanno scheme was applied for geometry optimization. The location of the transition state was determined using the climbing image nudged elastic band (CI-NEB) method.<sup>35</sup> Vibration analysis was used to ensure that there was only one imaginary frequency in each transition state. A six-layer slab of  $\text{Cu}_2\text{O}(111)$  was chosen to represent the surface.<sup>36</sup> It was modeled as a  $2 \times 2$  super unit containing 128 atoms. The bottom three layers were fixed throughout the calculations. The size of the simulated box was  $10.458 \times 12.067 \times 40.000\ \text{\AA}^3$  with periodic boundaries along  $\{X, Y, Z\}$

directions. The adsorption energy  $E_{\text{ad}}$  was calculated as  $E_{\text{ad}} = E_{\text{system}} - (E_{\text{cat}} + E_{\text{gas}})$ , where  $E_{\text{cat}}$ ,  $E_{\text{gas}}$ , and  $E_{\text{system}}$  correspond to the internal energy at 0 K of the catalyst slab, gas-phase molecule or atom, and the adsorption system at their ground states. A positive value indicates that the adsorption process is endothermic. The top sites over unsaturated and saturated surface Cu and O atoms are selected for adsorption tests. At each site, adsorbates in different orientations toward the catalyst surface are calculated, and the stable one with a higher  $E_{\text{ad}}$  is finally recorded. Elementary reactions considered in this study are selected according to the results of catalyst surface characterization, isotope-tracing experiments, and reported studies with Cu-based catalysts or using similar catalyst structures.<sup>11</sup>

### 3. RESULTS AND DISCUSSION

**3.1. Catalytic Performance.** Based on controlled experiments, i.e., investigation of Cu-based catalysts (Figure S2) and reaction conditions (Figures S3 and S4) in CO<sub>2</sub> hydrogenation, we found that the Cu<sub>2</sub>O/CeO<sub>2</sub> catalyst was capable of driving CO<sub>2</sub> hydrogenation to produce not only CH<sub>3</sub>OH but also C<sub>2</sub>H<sub>5</sub>OH with relatively higher selectivity. Details of materials and methods are shown in the Supporting Information. We systematically investigated the performance of the Cu<sub>2</sub>O/CeO<sub>2</sub> catalyst in plasma-assisted CO<sub>2</sub> hydrogenation to produce C<sub>2</sub>H<sub>5</sub>OH with the addition of H<sub>2</sub>O.

Figure 1a–c shows the effect of water content on product distribution, CO<sub>2</sub> conversion, and energy consumption for the production of C<sub>2</sub>H<sub>5</sub>OH and CH<sub>3</sub>OH over a Cu<sub>2</sub>O/CeO<sub>2</sub> catalyst. With increasing H<sub>2</sub>O content, the C<sub>2</sub>H<sub>5</sub>OH selectivity dramatically increases from 2.1 to 55.7%, while the CH<sub>3</sub>OH selectivity first slightly increases and then gradually decreases (Figure 1a). The CO<sub>2</sub> conversion shows a trend similar to the CH<sub>3</sub>OH selectivity (Figure 1b). Hence, the addition of a low content of water (H<sub>2</sub>O/CO<sub>2</sub> molar ratio below 0.5) favors CH<sub>3</sub>OH formation and CO<sub>2</sub> conversion, which is consistent with earlier reports<sup>17,18</sup> and our previous results.<sup>20</sup> A higher content of water promotes the selectivity of C<sub>2</sub>H<sub>5</sub>OH. However, under this condition (molar ratio of H<sub>2</sub>O/CO<sub>2</sub> = 2/1), the CO<sub>2</sub> conversion decreases by one-third. This reduction may be caused not only by the lower discharge voltages (Figure S5) but also by the electron affinity of water, capturing electrons, which reduces the electron density in the plasma. Consequently, the rate of electron impact reactions decreases, slowing the rate of CO<sub>2</sub> dissociation. We have summarized the production rates of different products under various reaction conditions in Table S2. Figures S6–S8 illustrate the gas chromatographic data, carbon balance, and catalyst stability testing. It should be noted that we also observed the promotion of C<sub>2</sub>H<sub>5</sub>OH formation by water on Cu<sub>2</sub>O/Al<sub>2</sub>O<sub>3</sub>, Cu<sub>2</sub>O/SiO<sub>2</sub>, and Cu<sub>2</sub>O/Fe<sub>2</sub>O<sub>3</sub> catalysts (Figure S9). As shown in Figures 1b and S9, there is clearly a trade-off between high C<sub>2</sub>H<sub>5</sub>OH selectivity at low CO<sub>2</sub> conversion upon more water addition, vs low C<sub>2</sub>H<sub>5</sub>OH selectivity at high CO<sub>2</sub> conversion with lower water content.

Overall, the selectivity toward alcohols (CH<sub>3</sub>OH and C<sub>2</sub>H<sub>5</sub>OH) substantially improves by the presence of H<sub>2</sub>O molecules on the Cu<sub>2</sub>O/CeO<sub>2</sub> catalyst, and 78.0% alcohols selectivity (22.3% CH<sub>3</sub>OH and 55.7% C<sub>2</sub>H<sub>5</sub>OH) is achieved in the case of H<sub>2</sub>O/CO<sub>2</sub> = 2/1. The energy consumption for alcohols formation also drops upon water addition in the case of the Cu<sub>2</sub>O/CeO<sub>2</sub> catalyst (Figure 1c), and the lowest energy consumption reaches 16.4 kJ/mmol for the H<sub>2</sub>O/CO<sub>2</sub> molar

ratio of 1.5. The CO selectivity from CO<sub>2</sub> hydrogenation at various water contents on Cu-based catalysts with different supports is shown in Figure S10, and the Cu<sub>2</sub>O/CeO<sub>2</sub> catalyst displays the lowest CO selectivity of all catalysts. In addition, control experiments indicate that the Cu<sub>2</sub>O/CeO<sub>2</sub> catalyst cannot activate CO<sub>2</sub> via H<sub>2</sub>O in the absence of H<sub>2</sub> (Figure S11). Similar investigations carried out under both plasma and nonplasma conditions, as depicted in Figure S12, demonstrate that CO<sub>2</sub> cannot be converted at 75 °C and atmospheric pressure without the assistance of plasma. This underscores the crucial role of plasma and hydrogen in catalytic reactions.

Figure 1d compares the product selectivity and CO<sub>2</sub> conversion for plasma-only, plasma + CeO<sub>2</sub>, and plasma + Cu<sub>2</sub>O/CeO<sub>2</sub> catalysts with and without H<sub>2</sub>O addition (0–1 and 2–1 denote the H<sub>2</sub>O/CO<sub>2</sub> molar ratio), and Figure S13 shows the corresponding energy consumption for alcohols production. In the absence of catalysts (plasma-only), C<sub>2</sub>H<sub>5</sub>OH is not observed in the products, which indicates that the C–C coupling reaction cannot be triggered in H<sub>2</sub>/CO<sub>2</sub> plasma without the assistance of catalysts, regardless of H<sub>2</sub>O. After the plasma was packed with the CeO<sub>2</sub> support (plasma + CeO<sub>2</sub>), there was a slight increase in CO<sub>2</sub> conversion, but the combination of CeO<sub>2</sub> packing and H<sub>2</sub>O addition led to a clear C<sub>2</sub>H<sub>5</sub>OH production (10.5% selectivity). More interestingly, in the case of packing the plasma with the Cu<sub>2</sub>O/CeO<sub>2</sub> catalyst (plasma + Cu<sub>2</sub>O/CeO<sub>2</sub>), the coupling of Cu<sub>2</sub>O/CeO<sub>2</sub> packing and H<sub>2</sub>O addition results in a dramatic enhancement of the C<sub>2</sub>H<sub>5</sub>OH selectivity (55.7%), which suggests a clear synergy among plasma, Cu<sub>2</sub>O/CeO<sub>2</sub> catalyst, and H<sub>2</sub>O molecules in promoting the C–C coupling reaction for C<sub>2</sub>H<sub>5</sub>OH production from CO<sub>2</sub> hydrogenation.

Figure 1e shows the temporal profiles of MS signals with different  $m/z$  values in CO<sub>2</sub> hydrogenation through plasma catalysis over the Cu<sub>2</sub>O/CeO<sub>2</sub> catalyst with intermittent addition of H<sub>2</sub>O (molar ratio of H<sub>2</sub>O/CO<sub>2</sub> = 2/1). In the initial stage, i.e., after plasma on but before H<sub>2</sub>O injection, the intensities of  $m/z = 31$  (CH<sub>3</sub>O and CH<sub>2</sub>OH) and  $m/z = 32$  (CH<sub>3</sub>OH) both show an increase, indicative of the production of CH<sub>3</sub>OH. The signal fluctuations observed at  $m/z = 45$  (CH<sub>3</sub>CH<sub>2</sub>O) can be deemed negligible owing to the low selectivity of C<sub>2</sub>H<sub>5</sub>OH. It should be noted that the catalyst was prerduced for the experiments, which explains why there was initially no increase in the signal value. Following each water injection, a sharp increase in  $m/z = 31$ , 32, and 45 suggests additional CH<sub>3</sub>OH and C<sub>2</sub>H<sub>5</sub>OH generation, enhancing the alcohols synthesis ( $m/z = 31$  is the primary signal for C<sub>2</sub>H<sub>5</sub>OH, indicative of fragmentation, while  $m/z = 45$  represents a secondary signal). After each termination of H<sub>2</sub>O injection, the intensity at  $m/z = 45$  (CH<sub>3</sub>CH<sub>2</sub>O) nearly reverts to its initial level, suggesting minimal C<sub>2</sub>H<sub>5</sub>OH production in the CO<sub>2</sub>/H<sub>2</sub> plasma when H<sub>2</sub>O was not added. Furthermore, considering the prediction of Lustemberg et al. that water may occupy adsorption sites intended for CH<sub>3</sub>OH on the catalyst surface,<sup>37</sup> thereby promoting its desorption, we speculate that water, beyond its role in C–C coupling reactions, might also influence the desorption of C<sub>2</sub>H<sub>5</sub>OH, as detailed in Section 3.5.

**3.2. Diagnostics of CO<sub>2</sub>/H<sub>2</sub>(/H<sub>2</sub>O) Plasma.** Figure 2a compares the waveforms of the discharge current of plasma-only and plasma packed with the Cu<sub>2</sub>O/CeO<sub>2</sub> catalyst. The Cu<sub>2</sub>O/CeO<sub>2</sub> packing exhibits a somewhat higher intensity of discharge current compared to the plasma-only condition.

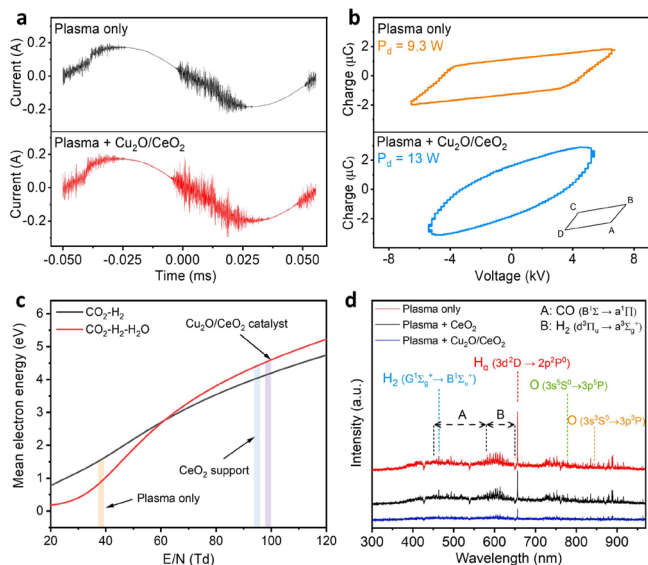


**Figure 2.** Results of plasma diagnostics. (a) Waveforms of discharge current and (b) Lissajous plots (AB and CD segments are the discharge-on phases, and the catalyst packing leads to an increase in their slopes) for plasma-only and plasma + Cu<sub>2</sub>O/CeO<sub>2</sub> catalyst. (c) Calculated mean electron energy as a function of the reduced electric field ( $E/N$ ; see text) for CO<sub>2</sub>/H<sub>2</sub> and CO<sub>2</sub>/H<sub>2</sub>/H<sub>2</sub>O plasma. (d) In situ OES results in CO<sub>2</sub>/H<sub>2</sub> plasma, for plasma-only, plasma + CeO<sub>2</sub> support, and plasma + Cu<sub>2</sub>O/CeO<sub>2</sub> catalyst. [Pd in (b) is discharge power, input power = 23 W].

Figure 2b shows the Lissajous plots corresponding to discharges of nonpacked plasma and plasma packed with the Cu<sub>2</sub>O/CeO<sub>2</sub> catalyst. The shape of the Lissajous plots changes from a parallelogram (no packing) to an oval shape (packed with Cu<sub>2</sub>O/CeO<sub>2</sub> catalysts), which is attributed to the increase in equivalent capacitance of the system with the addition of different materials.<sup>38</sup> Obviously, the slope of the discharge part in the plasma packing system is larger than that in the nonpacked system, corresponding to more discharge filaments, as also observed in (a), with a higher discharge efficiency ( $P_{\text{plasma-only}} = 9.3$  W and  $P_{\text{plasma+Cu2O/CeO2}} = 13$  W for the same input power of 23 W). Filamentary discharges are commonly beneficial for the electron density, and a higher intensity of the discharge current leads to a higher density of energetic electrons in the discharge area, which increases the possibility for activation, dissociation, and ionization of the feedstock gases through inelastic collisions with energetic electrons.

We calculated the mean electron energy and the electron energy distribution function (EEDF) for the CO<sub>2</sub>/H<sub>2</sub> plasma with and without H<sub>2</sub>O via Bolsig+, following a method proposed by Mei et al.<sup>39,40</sup> The mean electron energy is plotted as a function of the reduced electric field ( $E/N$ , i.e., the ratio of electric field over gas number density, expressed in Td, where 1 Td = 10<sup>-21</sup> V m<sup>2</sup>) in Figure 2c. The  $E/N$ , and thus the mean electron energy, of the packed plasma (by CeO<sub>2</sub> or Cu<sub>2</sub>O/CeO<sub>2</sub>) is much higher than that of plasma-only (no packing), mainly owing to the reduction in the gas-phase volume in the case of packing, causing the potential drop over a shorter distance and thus a stronger electric field as well as electric field enhancement due to packing polarization.<sup>41</sup> Besides, EEDFs in Figure S14 demonstrate that there are more electrons with higher energy in the packed plasmas. H<sub>2</sub>O addition slightly increases the fraction of high-energy electrons. In this regard, more reactive species are generated in the

packed plasma upon electron impact dissociation, excitation, and ionization of the feedstock molecules, enabling more significant reactions in the gas phase and at the catalyst surface.<sup>40</sup>

Finally, we applied in situ optical emission spectroscopy (OES) to detect important plasma species. Figure 2d illustrates several spectral lines and two spectral bands, including the H <sub>$\alpha$</sub>  line (656.3 nm, 3d<sup>2</sup>D → 2p<sup>2</sup>P<sup>0</sup>), the H<sub>2</sub> line (463 nm, G<sup>1</sup> $\tilde{a}_g^+$  → B<sup>1</sup> $\tilde{a}_u^+$ ), two O atomic spectral lines (777.5 nm, 3s<sup>5</sup>S<sup>0</sup> → 3p<sup>5</sup>P and 844.7 nm, 3s<sup>3</sup>S<sup>0</sup> → 3p<sup>3</sup>P), the CO band (450–580 nm, B<sup>1</sup> $\tilde{a} \rightarrow A^1$ P), and the H<sub>2</sub> band (580–650 nm, d<sup>3</sup>P<sub>u</sub> → a<sup>3</sup> $\tilde{a}_g^+$ ).<sup>42,43</sup> Clearly, plasma-only shows the highest signal intensity. Compared with plasma-only, the signal intensity is reduced by packing the CeO<sub>2</sub> support in the plasma, which is attributed to the shielding effect, and the signal intensity is further reduced by the Cu<sub>2</sub>O/CeO<sub>2</sub> packing, indicating that some active species are adsorbed by the Cu<sub>2</sub>O/CeO<sub>2</sub> catalyst. In addition, Figure S15a shows a decreasing signal intensity with an increasing H<sub>2</sub>O/CO<sub>2</sub> molar ratio. This is probably caused by the ionization of H<sub>2</sub>O, which consumes more energy, with correspondingly less energy to activate CO<sub>2</sub> and H<sub>2</sub>, thereby leading to a drop in CO<sub>2</sub> conversion (Figure 1b,d). Furthermore, the electronegativity of H<sub>2</sub>O results in more electron attachment, indicating a lower density of free electrons in the plasma and hence a lower production of reactive plasma species (Figure S15a), which may be another reason for the drop in CO<sub>2</sub> conversion.

To further verify the existence of OH radicals in the gas phase, OES measurements were conducted under plasma-only conditions (Figure S15b). A distinct OH emission peak at 309.5 nm was observed, particularly at a H<sub>2</sub>O/CO<sub>2</sub> molar ratio of 2, confirming the presence of OH radicals in the gas phase. The detection of OH radicals further supports their key role in driving surface reactions such as CO<sub>2</sub> reduction and H<sub>2</sub> activation under plasma conditions. The lifetime and density of OH radicals in plasma largely depend on the discharge mode and gas composition. Previous studies show that the density of OH radicals typically ranges from 10<sup>16</sup> to 10<sup>13</sup> cm<sup>-3</sup>, with 0.05–1% H<sub>2</sub>O content in the gas phase,<sup>44,45</sup> and their lifetime varies between 0.15 and 200  $\mu$ s.<sup>46,47</sup> In our study, the high content of H<sub>2</sub>O (33.33%) and the intensive filamentary discharge likely lead to abundant OH radicals, with a lifetime sufficient to drive surface reactions via E-R and L-H mechanisms.

### 3.3. Characterization of the Cu<sub>2</sub>O/CeO<sub>2</sub> Catalyst.

Powder X-ray diffraction (PXRD) patterns (Figure 3a) of the Cu<sub>2</sub>O/CeO<sub>2</sub> catalyst and CeO<sub>2</sub> support are highly consistent for both fresh and spent catalysts, indicating that loading copper on the CeO<sub>2</sub> support does not affect the crystal structure of CeO<sub>2</sub>. However, two weak diffraction peaks belonging to CuO, i.e., (111) and (-111) lattice plane, appear in the PXRD patterns of the Cu<sub>2</sub>O/CeO<sub>2</sub> catalyst, which may be attributed to the low loading of copper on the support (5 wt % loading). The H<sub>2</sub>-TPR (temperature-programmed reduction) profiles in Figure 3b display three different reduction peaks of copper-oxide species ( $\alpha$ ,  $\beta$ , and  $\gamma$ ) in both fresh and spent catalysts. The  $\alpha$  and  $\beta$  peaks are attributed to the reduction in highly dispersed CuO and Cu–O<sub>x</sub>–Ce solid solutions, respectively. CeO<sub>2</sub> has been found to promote the reduction in highly dispersed CuO, i.e., the smaller the CuO particles, the more easily can they be reduced.<sup>48</sup> The  $\gamma$  peak represents bulk CuO, which needs to be reduced at a higher

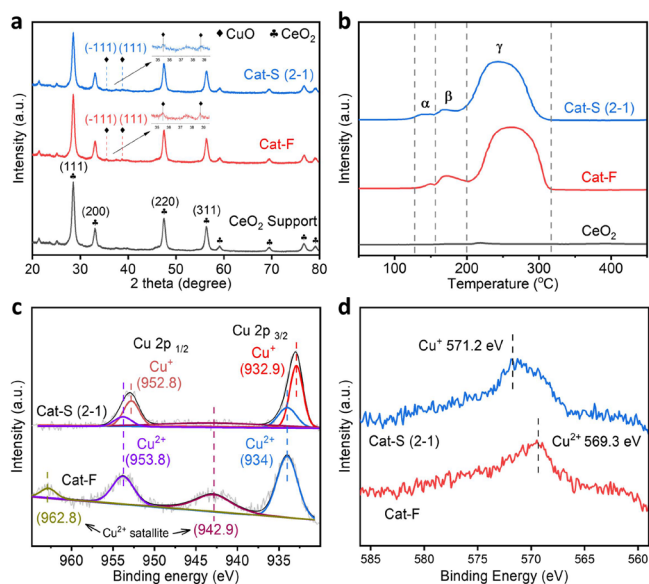


**Figure 3.** Characterization results of the  $\text{Cu}_2\text{O}/\text{CeO}_2$  catalysts with 5 wt % loading. (a) PXRD patterns. (b)  $\text{H}_2$ -TPR profiles. (c) Cu 2p XPS results. (d) Cu LMM Auger spectra. (Cat-F and Cat-S denote fresh and spent catalysts, respectively, and 2–1 denotes the molar ratio of  $\text{H}_2\text{O}/\text{CO}_2$ ).

temperature, indicating that most copper exists as large copper-oxide particles.

We also characterized the  $\text{Cu}_2\text{O}/\text{CeO}_2$  catalyst using HAADF-STEM and EDX mapping (Figure S16), which indicates a low dispersion of copper on  $\text{CeO}_2$ . The particle size distribution of CuO in the  $\text{Cu}_2\text{O}/\text{CeO}_2$  catalyst is illustrated in Figure S17 with an average CuO particle size of about 500 nm. This is consistent with PXRD and  $\text{H}_2$ -TPR results of Figure 3a, b, and the reasons for poor dispersion could be attributed to the low surface area of  $\text{CeO}_2$  and the high calcination temperature during catalyst preparation. The XPS result of Cu 2p (Figure 3c) illustrates that Cu species on the fresh catalyst are present in the form of CuO. On the spent catalyst, however, the Cu species change from CuO (934 and 953.8 eV) to  $\text{Cu}_2\text{O}$  (932.9 and 952.8 eV),<sup>49</sup> which may be caused by the reduction capability of  $\text{H}_2$  plasma during the reaction (Table S3). The observed decrease in the intensity of  $\text{Cu}^{2+}$  satellite peaks (942.9 and 962.8 eV) on the spent catalyst also provides evidence for the transformation of CuO to  $\text{Cu}_2\text{O}$ . The Cu LMM Auger spectra, shown in Figure 3d, further demonstrate the formation of the  $\text{Cu}_2\text{O}$  phase during the reaction.<sup>50</sup> However, the PXRD pattern only shows the CuO phase in the spent  $\text{Cu}_2\text{O}/\text{CeO}_2$  catalyst, which means that only the surface CuO layer is reduced to  $\text{Cu}_2\text{O}$  by  $\text{H}_2$  plasma. Subsequently,  $\text{Ar}^+$  is used to etch the spent  $\text{Cu}_2\text{O}/\text{CeO}_2$  catalyst with a depth of ca. 10 nm. However, the XPS result of Cu 2p shows only  $\text{Cu}^+$  species (Figure S18). Therefore,  $\text{Cu}_2\text{O}$  species could be the active sites of the  $\text{Cu}_2\text{O}/\text{CeO}_2$  catalyst for the hydrogenation of  $\text{CO}_2$  to  $\text{C}_2\text{H}_5\text{OH}$ .

To further support the above-mentioned conclusion, the fresh catalyst is first reduced by hydrogen to  $\text{Cu}^0$  species, followed by its further use in the  $\text{CO}_2$  hydrogenation reaction. The  $\text{Cu}^0$  species are oxidized to the  $\text{Cu}^+$  species (Figure S19), which can be attributed to the oxidizing properties of  $\text{H}_2\text{O}$  and  $\text{CO}_2$ . Although  $\text{H}_2$  is a reducing gas, the gas temperature in the plasma is not sufficient to reduce  $\text{Cu}^+$  to  $\text{Cu}^0$ . Previous reports came to the same conclusion that  $\text{Cu}^0$  was not stable in  $\text{H}_2/$

$\text{CO}_2$  plasma at low temperatures.<sup>51</sup> The above catalyst characterization results indicate that the surface  $\text{Cu}_2\text{O}$  layer of the  $\text{Cu}_2\text{O}/\text{CeO}_2$  catalyst is the active phase for the hydrogenation of  $\text{CO}_2$  to  $\text{C}_2\text{H}_5\text{OH}$ . The  $\text{N}_2$  physisorption data are shown in Figure S20 and Table S4, indicating that the BET surface area and pore volume of the  $\text{Cu}_2\text{O}/\text{CeO}_2$  catalyst are very low. The spent  $\text{Cu}_2\text{O}/\text{CeO}_2$  catalysts after plasma reaction with different  $\text{H}_2\text{O}$  contents are further characterized by PXRD,  $\text{H}_2$ -TPR, and XPS (Figure S21), and the relevant results indicate that the content of  $\text{H}_2\text{O}$  during plasma-catalytic  $\text{CO}_2$  hydrogenation does not have an obvious effect on the crystal phase and valence state of the spent  $\text{Cu}_2\text{O}/\text{CeO}_2$  catalysts.

**3.4. Isotope-Tracing Experiments.** We used  $\text{D}_2\text{O}$  and  $\text{H}_2^{18}\text{O}$  for isotope-tracing experiments to further determine the role of water in the C–H bond in  $\text{CO}_2$  hydrogenation. The mass spectra of the products from  $\text{CO}_2$  hydrogenation in the presence of  $\text{H}_2\text{O}$  are shown in Figure S22a,b, which are highly consistent with the standard mass spectra of  $\text{CH}_3\text{OH}$  and  $\text{C}_2\text{H}_5\text{OH}$ .<sup>52</sup> Subsequently, trace amounts of  $\text{CH}_3\text{OH}$  and  $\text{C}_2\text{H}_5\text{OH}$  are added to a mixture of  $\text{H}_2\text{O}$  and  $\text{D}_2\text{O}$  (99%  $\text{H}_2\text{O}$ , 1%  $\text{D}_2\text{O}$ ) as a control experiment to verify the H–D exchange reaction. As shown in Figure S22c,d, obvious H–D exchange reactions take place between the alcohol molecules and  $\text{D}_2\text{O}$  resulting in the formation of  $\text{CH}_3\text{OD}$  and  $\text{C}_2\text{H}_5\text{OD}$  molecules, implying that the H–D exchange reaction mainly occurs between the OH group in the alcohols molecules and the  $\text{D}_2\text{O}$  molecule.

The mass spectra of the products from  $\text{CO}_2$  hydrogenation in the presence of  $\text{D}_2\text{O}$  are shown in Figure 4a,b, revealing  $\text{CDH}_2\text{OD}$ ,  $\text{CD}_2\text{HO}$ ,  $\text{C}_2\text{DH}_4\text{OD}$ , and  $\text{C}_2\text{D}_2\text{H}_3\text{OD}$  among the products besides the expected products with only one D atom, originating from the H–D exchange reaction in the OH group of the alcohols. This means that D replaced two or more H atoms in the alcohol molecules, indicating that D atoms from

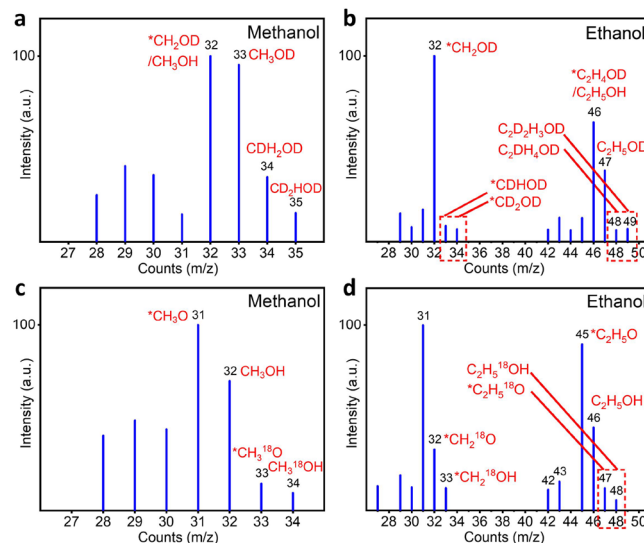


**Figure 4.** Isotope-tracing experimental results. (a, b) MS results of the products from  $\text{CO}_2$  hydrogenation over the  $\text{Cu}_2\text{O}/\text{CeO}_2$  catalyst in the presence of  $\text{D}_2\text{O}$ . (c, d) MS results of the products from  $\text{CO}_2$  hydrogenation over the  $\text{Cu}_2\text{O}/\text{CeO}_2$  catalyst in the presence of  $\text{H}_2^{18}\text{O}$ . Note that the  $m/z$  peaks for  $\text{CH}_3\text{OH}$  and  $\text{C}_2\text{H}_5\text{OH}$  typically correspond to different (fragmentation) species, hence the different assignments.

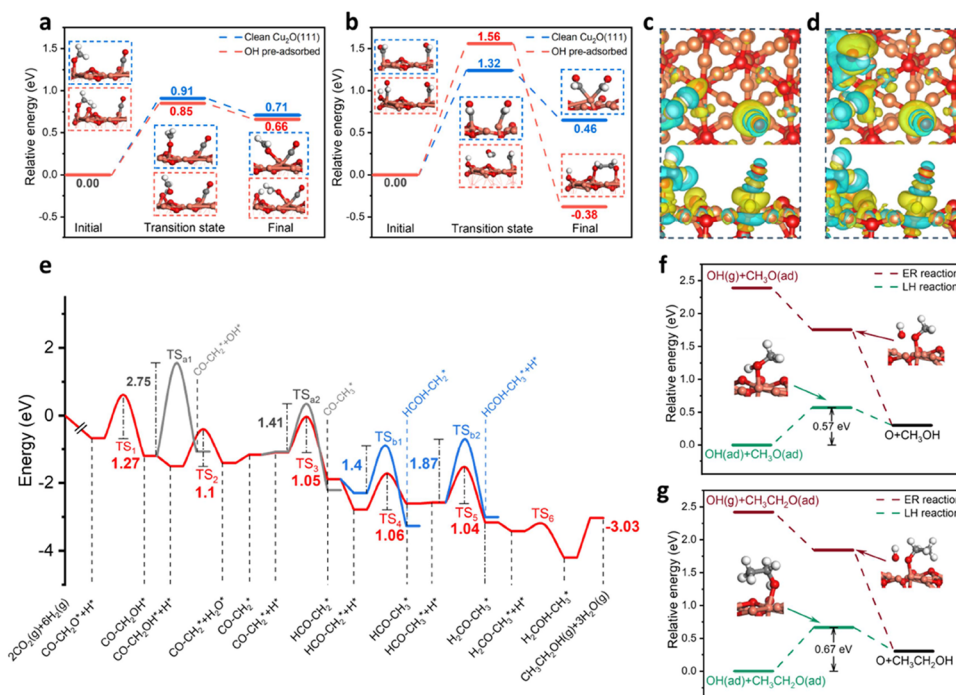


**Figure 5.** (a–e) DFT calculation results of C–C coupling. (a, b) Energy diagrams of C–C coupling at the  $\text{Cu}_{\text{cus}}$  sites on the surface of  $\text{Cu}_2\text{O}(111)$ : (a)  $\text{CO}^*-\text{H}_2\text{CO}^*$ ; (b)  $\text{HCO}^*-\text{HCO}^*$  coupling. (c, d) Partial charge distributions of  $(\text{OH}^-)\text{CO}-\text{H}_2\text{CO}$  before coupling: (c)  $\text{CO}-\text{H}_2\text{CO}$ ; (d)  $\text{OH}-\text{CO}-\text{H}_2\text{CO}$ . (e) Reaction pathway of  $\text{C}_2\text{H}_5\text{OH}$  formation from  $\text{CO}^*-\text{H}_2\text{CO}^*$  coupling (adsorbed species are labeled as \*). (f, g) Proton transfer of adsorbed  $\text{OH}^*$  or gas-phase OH to form (f)  $\text{CH}_3\text{OH}^*$  and (g)  $\text{C}_2\text{H}_5\text{OH}^*$ .

$\text{D}_2\text{O}$  dissociation are involved in the hydrogenation of  $\text{CO}_2$ , aside from the H–D exchange reaction. In other words, H from the dissociation of  $\text{H}_2\text{O}$  should also be involved in the hydrogenation of  $\text{CO}_2$  to  $\text{CH}_3\text{OH}$  and  $\text{C}_2\text{H}_5\text{OH}$ . In addition, the  $\text{H}_2/\text{D}_2\text{O}$  experiment demonstrates that H–D exchange also occurs between  $\text{H}_2$  and  $\text{D}_2\text{O}$  (Figure S23). The mass spectra of products from  $\text{CO}_2$  hydrogenation in the presence of  $\text{H}_2^{18}\text{O}$  are shown in Figure 4c, d, indicating that  $\text{CH}_3^{18}\text{OH}$  and  $\text{C}_2\text{H}_5^{18}\text{OH}$  are detected in the products. This means that a proportion of the OH group in  $\text{CH}_3\text{OH}$  and  $\text{C}_2\text{H}_5\text{OH}$  is derived from the OH species in the  $\text{H}_2\text{O}$  molecule. Electron paramagnetic resonance (EPR) results (Figure S24) further confirm the dissociation of  $\text{H}_2\text{O}$  into OH radicals in both  $\text{CO}_2/\text{H}_2\text{O}$  and  $\text{H}_2/\text{CO}_2/\text{H}_2\text{O}$  plasma systems. However, the OH signal is notably weaker in the presence of  $\text{H}_2$  ( $\text{H}_2/\text{CO}_2/\text{H}_2\text{O}$  plasma), suggesting that OH radicals are readily consumed under reducing conditions. However, the high content of  $\text{H}_2\text{O}$  likely facilitates a continuous dynamic process, where newly generated OH radicals from  $\text{H}_2\text{O}$  dissociation may compensate for the consumed OH radicals, maintaining the observed signals. In short, the isotope-tracing results and EPR analysis demonstrate that water dissociates into H and OH species, actively participating in the  $\text{CO}_2$  hydrogenation reaction under plasma conditions.

**3.5. DFT Calculations.** A six-layer  $\text{Cu}_2\text{O}(111)$  slab is built to simulate the C–C coupling and stepwise hydrogenation, as shown in Figure S25. Four typical sites, i.e., the surface-unsaturated Cu site ( $\text{Cu}_{\text{cus}}$ ), the saturated Cu site ( $\text{Cu}_{\text{csa}}$ ), the unsaturated O site ( $\text{O}_{\text{cus}}$ ), and the saturated O site ( $\text{O}_{\text{csa}}$ ), are tested and the  $\text{Cu}_{\text{cus}}$  site is the most stable adsorption site for the main reactants and intermediates. In this regard, the  $\text{Cu}_{\text{cus}}$  site is chosen as the active site for further reactions. The adsorption results and configurations are summarized in Table S5 and Figure S26.

Two typical C–C coupling mechanisms, i.e.,  $\text{CO}^*$  insertion into  $\text{CH}_3^*$  and the combination between  $\text{CH}_x\text{O}^*$ , are investigated.<sup>10,15,53–55</sup> The  $\text{CO}^*$  insertion is found to be unfavorable in this system due to the limited production of  $\text{CH}_3^*$ . A high barrier (2.05 eV) occurred in the decomposition of  $\text{CH}_3\text{OH}^*$  to  $\text{CH}_3^*$  and  $\text{OH}^*$  (Figure S27). Besides, the energy barrier for  $\text{CH}_3^*$  hydrogenation to  $\text{CH}_4^*$  (1.40 eV) is lower than that for the formation of  $\text{CH}_3\text{CO}^*$  (1.46 eV) by coupling with  $\text{CO}^*$  (Figure S28). The  $\text{CH}_3^*$  generation from  $\text{CO}_2$  hydrogenation and  $\text{CH}_4^*$  dissociation is limited due to the low  $\text{CH}_4$  selectivity (0.5% in this work) and the unfavorable route of  $\text{CO}_2$  to  $\text{CH}_3^*$  under plasma conditions.<sup>56</sup> Meanwhile, the barrier of the  $\text{CO}^*-\text{CH}_3^*$  coupling is higher than most barriers in the  $\text{CH}_x\text{O}^*-\text{CH}_x\text{O}^*$  coupling (Table S6). Accordingly, the  $\text{C}_2\text{H}_5\text{OH}$  formation via the CO insertion mechanism on  $\text{Cu}_2\text{O}(111)$  is quite difficult.

Abundant H and CO signals in the OES spectrum indicate the possible generation of  $\text{CH}_x\text{O}$  species and their C–C coupling.<sup>56</sup> Six possible C–C coupling reactions between  $\text{CH}_x\text{O}$  are tested at their most favorable coadsorption site, as shown in Figures 5a,b and S29, Tables S6 and S7. In contrast to the HCO–HCO coupling mechanism observed with the Cu–Cs catalyst,<sup>55</sup> the  $\text{CO}^*-\text{H}_2\text{CO}^*$  coupling in this study exhibits the lowest barrier of 0.91 eV over the  $\text{Cu}_{\text{cus}}$  site. Interestingly, only the  $\text{H}_2\text{CO}^*-\text{H}_2\text{CO}^*$  coupling shows an obvious C–C bonding (Figure S30), while other couplings show the coadsorption of two  $\text{CH}_x\text{O}^*$  molecules, which could be attributed to the coordination status of C–C atoms.

Figure 1a shows the switch effect of the highest selectivity of alcohols from methanol to ethanol when the  $\text{H}_2\text{O}/\text{CO}_2$  ratio reaches 1. At this time, the amount of  $\text{H}_2\text{O}$  added is much higher than its yield from the hydrogenation. In the plasma region, the H\* dissociated from  $\text{H}_2\text{O}$  dissociation plays a similar role as  $\text{H}_2$  for hydrogenation. Hence,  $\text{OH}^*$  is assumed

to be the main factor in promoting the production of  $C_2H_5OH$ . Two possible effects of hydroxyl groups, i.e.,  $OH^*$  preadsorption and the proton transfer inspired by Yang's work claiming that the catalyst surface is critical in the  $CO_2$  hydrogenation to  $C_2H_5OH$ ,<sup>57</sup> are investigated. The preadsorbed  $OH^*$  affects the C–C couplings.  $OH^*$  favors the neighbor  $Cu_{cus}$  site when it coadsorbs with C–C coupling species (Table S8 and Figure S31).  $OH^*$  lowers the barrier in the  $CO-H_2CO$  coupling from 0.91 to 0.85 eV, while it increases the barrier in the  $HCO-HCO$  coupling from 1.32 to 1.56 eV (Figure 5a). The preadsorption of  $OH^*$  at a neighboring  $Cu_{cus}$  site slightly changes the charge distribution near  $H_2CO^*$  and promotes its migration to bind with  $CO^*$  adsorbed  $Cu_{cus}$  (Table S9, Figures 5c, d, S32, and S33). In this regard, the preadsorption of  $OH^*$  could to a certain extent promote the C–C coupling via  $CO-H_2CO$ , showing a much lower barrier than the other five C–C coupling pathways (Table S6).

Considering  $CO^*-H_2CO^*$  as the main coupling way, the stepwise hydrogenation is shown in Figure 5e, with detailed information in Table S10.  $CO^*-H_2CO^*$  prefers to detach the O atom from  $-CH_2O$  via two hydrogenation steps to form  $H_2O$ , rather than via the direct decomposition of  $-CH_2OH^*$  to  $CH_2^*$  and  $OH^*$  ( $E_a = 2.75$  eV). Subsequently,  $CO^*-CH_2^*$  prefers hydrogenation to  $HCO^*-CH_2^*$  ( $E_a = 1.05$  eV) rather than to  $CO^*-CH_3^*$  ( $E_a = 1.41$  eV). Furthermore,  $H^*$  is more likely to react with  $-CH_2^*$  ( $E_a: 1.06$  eV) rather than with  $-HCO^*$  ( $E_a: 1.40$  eV) in the  $HCO^*-CH_2^*$  complex. Subsequently, the  $CH_3^*-HCO^*$  complex receives two  $H^*$  atoms to eventually form  $C_2H_5OH^*$ . The  $C_2H_5OH^*$  undergoes desorption to finalize the  $C_2H_5OH$  synthesis with a desorption energy of 1.17 eV. A compared path from  $HCO^*-HCO^*$  shows a higher rate-limiting step (1.60 eV) than the  $CO-H_2CO$  path (1.27 eV), as shown in Figure S34, which again proves the availability of the  $CO^*-H_2CO^*$  route.

According to isotope-tracing experiments, we proposed two possible reaction mechanisms for OH-induced alcohol synthesis. One is the proton transfer from OH to the alcohols. The other is the direct replacement of O in methoxyl and ethoxyl by OH. As shown in Figure 5f, g, the final steps of  $CH_3OH^*$  and  $C_2H_5OH^*$  formation are facilitated via the proton transfer. In the Langmuir–Hinshelwood (L-H) reactions,  $OH^*$  coadsorbs with  $CH_3O^*$  or  $CH_3CH_2O^*$  at the  $Cu_{cus}$  site, forming  $CH_3OH^*$  and  $C_2H_5OH^*$  with energy barriers of 0.57 and 0.67 eV, respectively. In the E-R reactions, the formation of  $CH_3OH^*$  and  $C_2H_5OH^*$  seems to have no obvious barrier due to the high reactivity of the  $OH(g)$  species. Besides, highly reactive gas-phase  $OH(g)$  species can move to the  $Cu_2O$  surface to react with  $CH_3O^*$  or  $CH_3CH_2O^*$ , forming  $CH_3OH^*$  and  $O^*$  or  $C_2H_5OH^*$  and  $O^*$ , respectively.  $E_a$  values for these two reactions are high, i.e., 1.50 eV for  $CH_3OH$  and 1.62 eV for  $C_2H_5OH$ , respectively, due to the stable C–O bonds in both methoxyl and ethoxyl (Figure S35). The above results indicate that the alcohol production promoted by OH radicals is more likely via the proton transfer.

Apart from the hydrogenation, the preadsorbed  $OH^*$  is found to facilitate the  $C_2H_5OH$  desorption. As shown in Table S11 and Figures S36 and S37, the coadsorption of  $H_2O^*$  and  $C_2H_5OH^*$  is more stable when  $H_2O^*$  is at the  $Cu_{cus}$  site, and then the  $C_2H_5OH^*$  is unbonded. In this case, the adsorption energy of  $C_2H_5OH^*$  is significantly reduced from  $-1.17$  to  $-0.71$  eV. By contrast, when  $C_2H_5OH^*$  is adsorbed at the  $Cu_{cus}$  site, the  $H_2O$  molecule shows physisorption near

$C_2H_5OH^*$ , and the adsorption energy of  $C_2H_5OH$  is slightly reduced to  $-1.13$  eV. Meanwhile, the competitive adsorption of  $OH^*$  at neighboring sites can easily get involved in the next C–C coupling and in the proton transfer processes after the desorption of  $C_2H_5OH$ .

Generally,  $H_2O$  acts as a “switch” in guiding  $CO_2$  hydrogenation from methanol to ethanol in Cu-based plasma-catalytic system. The multiple roles of  $H_2O$  in  $C_2H_5OH$  synthesis, namely, the C–C coupling enhancement, the proton transfer, and the desorption promotion, offer a competitive approach to green-chemical synthesis at room temperature and atmospheric pressure with a distributed power supply.<sup>58,59</sup> Additionally, the presence of water vapor stabilizes methanol and ethanol, shortening their residence time in the plasma phase by reducing their interaction with highly reactive plasma species, thereby preventing excessive decomposition. We note that the oxide-support interaction for  $Cu_2O-CeO_2$  might also be a factor affecting  $CO_2$  hydrogenation and alcohols selectivity.<sup>60</sup> However, in this work, the bulk  $CuO$  particle size is found to be very large, and the dispersion is very poor, leaving limited  $Cu-CeO_2$  interfacial sites for possible reactions. Meanwhile,  $CeO_2$  alone does not show a superior improvement in  $CO_2$  conversion performance compared with other oxides (Figure S9). In this regard, unlike  $H_2O$  addition, the  $CeO_2$  support might not be a determining factor in guiding C–C coupling and hydrogenation.

In this study, the energy consumption for the synthesis of alcohols was determined to be approximately 16.4 kJ/mmol, which is significantly higher than the heating value of ethanol as a fuel ( $\sim 1.23$  kJ/mmol). The low energy efficiency of our system is likely attributed to the inherent energy losses during plasma activation, including ineffective collisions and recombination of reactive species, as well as the generation of byproducts such as CO and  $CH_4$ . Future improvements could focus on optimizing catalysts for higher ethanol selectivity, refining reactor designs to minimize energy dissipation, and integrating energy recovery systems. Addressing these challenges is essential for advancing the viability of plasma-catalytic  $CO_2$  hydrogenation.

## 4. CONCLUSIONS

We demonstrated the synergy between plasma and  $Cu_2O/CeO_2$  catalyst in  $CO_2$  hydrogenation to alcohols with the assistance of  $H_2O$ . The nonthermal plasma enables the conversion of small molecules ( $CO_2$ ,  $H_2$ ,  $H_2O$ , etc.) over the  $Cu_2O/CeO_2$  catalyst under mild conditions, achieving a high  $C_2H_5OH$  selectivity of 56% at atmospheric pressure and  $\sim 75$  °C. The addition of water improves the energy efficiency by over 32 times compared to using plasma alone, and the dissociated H and OH from  $H_2O$  are found engaged in the  $CO_2$  hydrogenation. DFT calculations suggest that the C–C coupling via  $CO-H_2CO$  combination is most likely to happen at the unsaturated  $Cu_{cus}$  site with OH preadsorption over the  $Cu_2O$  (111) surface. Meanwhile, the OH species could promote stepwise hydrogenation due to the proton transfer via both L-H and E-R mechanisms. The competitive adsorption of  $H_2O$  and OH improves the alcohols desorption by “seizing” the  $Cu_{cus}$  sites. In summary, the triple role of  $H_2O$  on alcohols production, specifically the promotion of C–C coupling, hydrogenation, and alcohols desorption, makes it a switch in controlling alcohol generation from  $CH_3OH$  to  $C_2H_5OH$ . New insights in this work enable a better

understanding of CO<sub>2</sub> conversion to higher alcohols in plasma-catalysis.

## ■ ASSOCIATED CONTENT

### SI Supporting Information

The Supporting Information is available free of charge at <https://pubs.acs.org/doi/10.1021/acscatal.4c06543>.

Quantitative analysis of reaction results; schematic diagram of the experimental setup; summary of CO<sub>2</sub> hydrogenation to C<sub>2</sub>H<sub>5</sub>OH with various catalysts and catalytic methods; plasma diagnoses data (temperature distribution by IR camera, discharge parameters by oscilloscope, and active species by OES); reaction performance data (GC profiles and control experiments); carbon balance calculations; stability tests; energy consumption data; catalyst characterization data (HAADF-STEM, XPS, N<sub>2</sub> adsorption, TPR, GC-MS, isotope tracer, and EPR); electronic energy distribution function; and DFT calculation results (PDF)

## ■ AUTHOR INFORMATION

### Corresponding Authors

**Min Liu** – State Key Laboratory of Powder Metallurgy, School of Physics, Central South University, Changsha 410083, China; [orcid.org/0000-0002-9007-4817](https://orcid.org/0000-0002-9007-4817); Email: [minliu@csu.edu.cn](mailto:minliu@csu.edu.cn)

**Yi Liu** – State Key Laboratory of Fine Chemicals, School of Chemical Engineering, Dalian University of Technology, Dalian 116024, China; [orcid.org/0000-0002-2073-4832](https://orcid.org/0000-0002-2073-4832); Email: [diligenliu@dlut.edu.cn](mailto:diligenliu@dlut.edu.cn)

**An-Hui Lu** – State Key Laboratory of Fine Chemicals, School of Chemical Engineering, Dalian University of Technology, Dalian 116024, China; [orcid.org/0000-0003-1294-5928](https://orcid.org/0000-0003-1294-5928); Email: [anhuilu@dlut.edu.cn](mailto:anhuilu@dlut.edu.cn)

**Yanhui Yi** – State Key Laboratory of Fine Chemicals, School of Chemical Engineering, Dalian University of Technology, Dalian 116024, China; [orcid.org/0000-0002-5869-9382](https://orcid.org/0000-0002-5869-9382); Email: [yianhui@dlut.edu.cn](mailto:yianhui@dlut.edu.cn)

### Authors

**Shengyan Meng** – State Key Laboratory of Fine Chemicals, School of Chemical Engineering, Dalian University of Technology, Dalian 116024, China

**Zhaolun Cui** – Key Lab of Materials Modification by Laser, Ion, and Electron Beams, Dalian University of Technology, Dalian 116024, China; School of Electric Power Engineering, South China University of Technology, Guangzhou 510630, China

**Qian Chen** – State Key Laboratory of Fine Chemicals, School of Chemical Engineering, Dalian University of Technology, Dalian 116024, China

**Hang Zhang** – State Key Laboratory of Powder Metallurgy, School of Physics, Central South University, Changsha 410083, China

**Shangkun Li** – Research group PLASMANT, Department of Chemistry, University of Antwerp, BE-2610 Wilrijk-Antwerp, Belgium; [orcid.org/0000-0002-9297-1669](https://orcid.org/0000-0002-9297-1669)

**Erik Cornelis Neyts** – Research group PLASMANT, Department of Chemistry, University of Antwerp, BE-2610 Wilrijk-Antwerp, Belgium; [orcid.org/0000-0002-3360-3196](https://orcid.org/0000-0002-3360-3196)

**Evgenii Vlasov** – Electron Microscopy for Materials Science (EMAT), University of Antwerp, BE-2610 Wilrijk-Antwerp, Belgium

**Kellie Jenkinson** – Electron Microscopy for Materials Science (EMAT), University of Antwerp, BE-2610 Wilrijk-Antwerp, Belgium

**Sara Bals** – Electron Microscopy for Materials Science (EMAT), University of Antwerp, BE-2610 Wilrijk-Antwerp, Belgium

**Dezheng Yang** – Key Lab of Materials Modification by Laser, Ion, and Electron Beams, Dalian University of Technology, Dalian 116024, China; [orcid.org/0000-0002-8549-3507](https://orcid.org/0000-0002-8549-3507)

**Annemie Bogaerts** – Research group PLASMANT, Department of Chemistry, University of Antwerp, BE-2610 Wilrijk-Antwerp, Belgium; [orcid.org/0000-0001-9875-6460](https://orcid.org/0000-0001-9875-6460)

Complete contact information is available at: <https://pubs.acs.org/doi/10.1021/acscatal.4c06543>

### Author Contributions

<sup>▽</sup>S.M., Z.C., and Q.C. equally contributed to this work.

### Notes

The authors declare no competing financial interest.

## ■ ACKNOWLEDGMENTS

This work was supported by the National Natural Science Foundation of China (22272015, 22472018, and 21503032), the European Research Council (ERC) under the European Union's Horizon 2020 research and innovation programme (ERC Synergy grant 810182 SCOPE and 823717 ESTEEM3), and the Methusalem project at Universiteit Antwerpen. Computational resources were provided by the HPC core facility CalcUA of the Universiteit Antwerpen and VSC (Flemish Supercomputer Center).

## ■ REFERENCES

- (1) Von der Assen, N.; Voll, P.; Peters, M.; Bardow, A. Life cycle assessment of CO<sub>2</sub> capture and utilization: a tutorial review. *Chem. Rev.* **2014**, *43*, 7982–7994.
- (2) Porosoff, M. D.; Yang, X.; Boscoboinik, J. A.; Chen, J. G. Molybdenum Carbide as Alternative Catalysts to Precious Metals for Highly Selective Reduction of CO<sub>2</sub> to CO. *Angew. Chem., Int. Ed.* **2014**, *53*, 6705–6709.
- (3) Xu, D.; Wang, Y.; Ding, M.; Hong, X.; Liu, G.; Tsang, S. C. E. Advances in higher alcohol synthesis from CO<sub>2</sub> hydrogenation. *Chem.* **2021**, *7*, 849–881.
- (4) Li, Z.; Wang, J.; Qu, Y.; Liu, H.; Tang, C.; Miao, S.; Feng, Z.; An, H.; Li, C. Highly Selective Conversion of Carbon Dioxide to Lower Olefins. *ACS Catal.* **2017**, *7*, 8544–8548.
- (5) Ni, Y. M.; Chen, Z. Y.; Fu, Y.; Liu, Y.; Zhu, W. L.; Liu, Z. M. Selective conversion of CO<sub>2</sub> and H<sub>2</sub> into aromatics. *Nat. Commu.* **2018**, *9*, 3457.
- (6) Zhong, J.; Yang, X.; Wu, Z.; Liang, B.; Huang, Y.; Zhang, T. State of the art and perspectives in heterogeneous catalysis of CO<sub>2</sub> hydrogenation to methanol. *Chem. Soc. Rev.* **2020**, *49*, 1385–1413.
- (7) Sun, J.; Wang, Y. Recent Advances in Catalytic Conversion of Ethanol to Chemicals. *ACS Catal.* **2014**, *4*, 1078–1090.
- (8) Inoue, T.; Iizuka, T.; Tanabe, K. Hydrogenation of Carbon Dioxide and Carbon Monoxide over Supported Rhodium Catalysts under 10 bar Pressure. *Appl. Catal., A* **1989**, *46*, 1–9.
- (9) Wang, D.; Bi, Q.; Yin, G.; Wang, P.; Huang, F.; Xie, X.; Jiang, M. Photochemical Preparation of Anatase Titania Supported Gold Catalyst for Ethanol Synthesis from CO<sub>2</sub> Hydrogenation. *Catal. Lett.* **2018**, *148*, 11–22.

- (10) He, Z.; Qian, Q.; Ma, J.; Meng, Q.; Zhou, H.; Song, J.; Liu, Z.; Han, B. Water-Enhanced Synthesis of Higher Alcohols from CO<sub>2</sub> Hydrogenation over a Pt/Co<sub>3</sub>O<sub>4</sub> Catalyst under Milder Conditions. *Angew. Chem., Int. Ed.* **2016**, *55*, 737–741.
- (11) Bai, S.; Shao, Q.; Wang, P.; Dai, Q.; Wang, X.; Huang, X. Highly Active and Selective Hydrogenation of CO<sub>2</sub> to Ethanol by Ordered Pd-Cu Nanoparticles. *J. Am. Chem. Soc.* **2017**, *139*, 6827–6830.
- (12) Wang, L.; Wang, L.; Zhang, J.; Liu, X.; Wang, H.; Zhang, W.; Yang, Q.; Ma, J.; Dong, X.; Yoo, S. J.; Kim, J.-G.; Meng, X.; Xiao, F.-S. Selective Hydrogenation of CO<sub>2</sub> to Ethanol over Cobalt Catalysts. *Angew. Chem., Int. Ed.* **2018**, *57*, 6104–6108.
- (13) Yang, C.; Liu, S.; Wang, Y.; Song, J.; Wang, G.; Wang, S.; Zhao, Z.-J.; Mu, R.; Gong, J. The Interplay between Structure and Product Selectivity of CO<sub>2</sub> Hydrogenation. *Angew. Chem., Int. Ed.* **2019**, *58*, 11242–11247.
- (14) Ding, L.; Shi, T.; Gu, J.; Cui, Y.; Zhang, Z.; Yang, C.; Chen, T.; Lin, M.; Wang, P.; Xue, N.; Peng, L.; Guo, X.; Zhu, Y.; Chen, Z.; Ding, W. CO<sub>2</sub> Hydrogenation to Ethanol over Cu@Na-Beta. *Chem.* **2020**, *6*, 2673–2689.
- (15) Zhang, S.; Liu, X.; Shao, Z.; Wang, H.; Sun, Y. Direct CO<sub>2</sub> hydrogenation to ethanol over supported Co<sub>2</sub>C catalysts: Studies on support effects and mechanism. *J. Catal.* **2020**, *382*, 86–96.
- (16) Zhang, S.; Wu, Z.; Liu, X.; Shao, Z.; Xia, L.; Zhong, L.; Wang, H.; Sun, Y. Tuning the interaction between Na and Co<sub>2</sub>C to promote selective CO<sub>2</sub> hydrogenation to ethanol. *Appl. Catal., B* **2021**, *293*, No. 120207.
- (17) Jiang, X.; Nie, X.; Gong, Y.; Moran, C. M.; Wang, J.; Zhu, J.; Chang, H.; Guo, X.; Walton, K. S.; Song, C. A combined experimental and DFT study of H<sub>2</sub>O effect on In<sub>2</sub>O<sub>3</sub>/ZrO<sub>2</sub> catalyst for CO<sub>2</sub> hydrogenation to methanol. *J. Catal.* **2020**, *383*, 283–296.
- (18) Wang, Y.; Gao, W.; Li, K.; Zheng, Y.; Xie, Z.; Na, W.; Chen, J. G.; Wang, H. Strong Evidence of the Role of H<sub>2</sub>O in Affecting Methanol Selectivity from CO<sub>2</sub> Hydrogenation over Cu-ZnO-ZrO<sub>2</sub>. *Chem.* **2020**, *6*, 419–430.
- (19) Graciani, J.; Grinter, C.; Ramirez, J.; Palomino, R.; Xu, F.; Waluyo, I.; Stacchiola, D.; Sanz, J.; Senanayake, S.; Rodriguez, J. Conversion of CO<sub>2</sub> to Methanol and Ethanol on Pt/CeO<sub>x</sub>/TiO<sub>2</sub> (110): Enabling Role of Water in C-C Bond Formation. *ACS Catal.* **2022**, *12*, 15097–15109.
- (20) Cui, Z.; Meng, S.; Yi, Y.; Jafarzadeh, A.; Li, S.; Neyts, E. C.; Hao, Y.; Li, L.; Zhang, X.; Wang, X.; Bogaerts, A. Plasma-Catalytic Methanol Synthesis from CO<sub>2</sub> Hydrogenation over a Supported Cu Cluster Catalyst: Insights into the Reaction Mechanism. *ACS Catal.* **2022**, *12*, 1326–1337.
- (21) da Silva, A. H.M.; Vieira, L. H.; Santanta, C. S.; Koper, M. T.M.; Assaf, E. M.; Assaf, J. M.; Gomes, J. F. Ethanol formation from CO<sub>2</sub> hydrogenation at atmospheric pressure using Cu catalysts: Water as a key component. *Appl. Catal. B* **2023**, *324*, 122221.
- (22) Snoeckx, R.; Bogaerts, A. Plasma technology—a novel solution for CO<sub>2</sub> conversion. *Chem. Soc. Rev.* **2017**, *46*, S805–S863.
- (23) Kim, D.-Y.; Ham, H.; Chen, X.; Liu, S.; Xu, H.; Lu, B.; Furukawa, S.; Kim, H.-H.; Takakusagi, S.; Sasaki, K.; Nozaki, T. Cooperative catalysis of vibrationally excited CO<sub>2</sub> and alloy catalyst breaks the thermodynamic equilibrium limitation. *J. Am. Chem. Soc.* **2022**, *144*, 14140–14149.
- (24) Gao, X.; Liang, J.; Wu, L.; Wu, L.; Kawi, S. Dielectric Barrier Discharge Plasma-Assisted Catalytic CO<sub>2</sub> Hydrogenation: Synergy of Catalyst and Plasma. *Catalysts* **2022**, *12*, 66.
- (25) Xu, S.; Chen, H.; Fan, X. Rational design of catalysts for non-thermal plasma (NTP) catalysis: A reflective review. *Catal. Today* **2023**, *419*, 114144.
- (26) Bogaerts, A.; Tu, X.; Whitehead, J. C.; Centi, G.; Lefferts, L.; Guitella, O.; Azzolina-Jury, F.; Kim, H. H.; Murphy, A.; Schneider, W.; Nozaki, T.; Hicks, J.; Rousseau, A.; Thevenet, F.; Khacef, A.; Cerreon, M. The 2020 plasma catalysis roadmap. *J. Phys. D: Appl. Phys.* **2020**, *53*, 443001.
- (27) Shirazi, M.; Neyts, E. C.; Bogaerts, A. DFT study of Ni-catalyzed plasma dry reforming of methane. *Appl. Catal., B* **2017**, *205*, 605–614.
- (28) Hutter, J.; Iannuzzi, M.; Schiffmann, F.; VandeVondele, J. CP2K: atomistic simulations of condensed matter systems. *Wiley Interdiscip. Rev. Comput. Mol. Sci.* **2014**, *4*, 15–25.
- (29) VandeVondele, J.; Krack, M.; Mohamed, F.; Parrinello, M.; Chassaing, T.; Hutter, J. QUICKSTEP: Fast and accurate density functional calculations using a mixed Gaussian and plane waves approach. *Comput. Phys. Commun.* **2005**, *167*, 103–128.
- (30) VandeVondele, J.; Hutter, J. Gaussian basis sets for accurate calculations on molecular systems in gas and condensed phases. *J. Chem. Phys.* **2007**, *127*, 114105.
- (31) Goedecker, S.; Teter, M.; Hutter, J. Separable dual-space Gaussian pseudopotentials. *Phys. Rev. B* **1996**, *54*, 1703–1710.
- (32) Grimme, S.; Ehrlich, S.; Goerigk, L. Effect of the Damping Function in Dispersion Corrected Density Functional Theory. *J. Comput. Chem.* **2011**, *32*, 1456–1465.
- (33) Grimme, S.; Antony, J.; Ehrlich, S.; Krieg, H. A consistent and accurate ab initio parametrization of density functional dispersion correction (DFT-D) for the 94 elements H-Pu. *J. Chem. Phys.* **2010**, *132*, 154104.
- (34) Bal, K. M.; Huygh, S.; Bogaerts, A.; Neyts, E. C. Effect of plasma-induced surface charging on catalytic processes: application to CO<sub>2</sub> activation. *Plasma Sources Sci. Technol.* **2018**, *27*, No. 024001.
- (35) Henkelman, G.; Uberuaga, B. P.; Jonsson, H. A climbing image nudged elastic band method for finding saddle points and minimum energy paths. *J. Chem. Phys.* **2000**, *113*, 9901–9904.
- (36) Song, Y.-Y.; Wang, G.-C. A DFT Study and Microkinetic Simulation of Propylene Partial Oxidation on CuO (111) and CuO (100) Surfaces. *J. Phys. Chem. C* **2016**, *120*, 27430–27442.
- (37) Lustemberg, P. G.; Palomino, R. M.; Gutierrez, R. A.; Grinter, D. C.; Vorokhta, M.; Liu, Z.; Ramirez, P. J.; Matolin, V.; Veronica Ganduglia-Pirovano, M.; Senanayake, S. D.; Rodriguez, J. A. Direct Conversion of Methane to Methanol on Ni-Ceria Surfaces: Metal-Support Interactions and Water-Enabled Catalytic Conversion by Site Blocking. *J. Am. Chem. Soc.* **2018**, *140*, 7681–7687.
- (38) Butterworth, T.; Allen, R. W. K. Plasma-catalyst interaction studied in a single pellet DBD reactor: dielectric constant effect on plasma dynamics. *Plasma Sources Sci. Technol.* **2017**, *26*, No. 065008.
- (39) Hagelaar, G. J. M.; Pitchford, L. C. Solving the Boltzmann equation to obtain electron transport coefficients and rate coefficients for fluid models. *Plasma Sources Sci. Technol.* **2005**, *14*, 722–733.
- (40) Mei, D. H.; Zhu, X. B.; He, Y. L.; Yan, J. D.; Tu, X. Plasma-assisted conversion of CO<sub>2</sub> in a dielectric barrier discharge reactor: understanding the effect of packing materials. *Plasma Sources Sci. Technol.* **2015**, *24*, No. 015011.
- (41) Van Laer, K.; Bogaerts, A. Fluid modelling of a packed bed dielectric barrier discharge plasma reactor. *Plasma Sources Sci. Technol.* **2016**, *25*, No. 015002.
- (42) Meng, S.; Wu, L.; Liu, M.; Cui, Z.; Chen, Q.; Li, S.; Yan, J.; Wang, L.; Wang, X.; Qian, J.; Guo, H.; Niu, J.; Bogaerts, A.; Yi, Y. Plasma-driven CO<sub>2</sub> hydrogenation to CH<sub>3</sub>OH over Fe<sub>2</sub>O<sub>3</sub>/γ-Al<sub>2</sub>O<sub>3</sub> catalyst. *AIChE J.* **2023**, *69*, No. e18154.
- (43) Chen, Q.; Meng, S.; Liu, R.; Zhai, X.; Wang, X.; Wang, L.; Guo, H.; Yi, Y. Plasma-catalytic CO<sub>2</sub> hydrogenation to methanol over CuO-MgO/Beta catalyst with high selectivity. *Appl. Catal., B* **2024**, *342*, No. 123422.
- (44) Benedikt, J.; Schroeder, D.; Schneider, S.; Willems, G.; Pajdarova, A.; Vlcek, J.; Schulz-von der Gathen, V. Absolute OH and O radical densities in effluent of a He/H<sub>2</sub>O micro-scaled atmospheric pressure plasma jet. *Plasma Sources Sci. T.* **2016**, *25*, No. 045013.
- (45) Li, D.; Nikiforov, A.; Britun, N.; Snyders, R.; Kong, M. G.; Leys, C. OH radical production in an atmospheric pressure surface micro-discharge array. *J. Phys. D: Appl. Phys.* **2016**, *49*, 455202.
- (46) Piskarev, I. M. The Formation of Ozone-Hydroxyl Mixture in Corona Discharge and Lifetime of Hydroxyl Radicals. *IEEE Trans. Plasma Sci.* **2021**, *49*, 1363–1372.

(47) Pei, X.; Lu, Y.; Wu, S.; Xiong, Q.; Lu, X. A study on the temporally and spatially resolved OH radical distribution of a room-temperature atmospheric-pressure plasma jet by laser-induced fluorescence imaging. *Plasma Sources Sci. T.* **2013**, *22*, No. 025023.

(48) He, C.; Yu, Y.; Yue, L.; Qiao, N.; Li, J.; Shen, Q.; Yu, W.; Chen, J.; Hao, Z. Low-temperature removal of toluene and propanal over highly active mesoporous CuCeO<sub>x</sub> catalysts synthesized via a simple self-precipitation protocol. *Appl. Catal., B* **2014**, *147*, 156–166.

(49) Zhang, X. L.; Li, G. J.; Tian, R. L.; Feng, W. J.; Wen, L. Monolithic porous CuO/CeO<sub>2</sub> nanorod composites prepared by dealloying for CO catalytic oxidation. *J. Alloys Compd.* **2020**, *826*, No. 154149.

(50) Platzman, I.; Brener, R.; Haick, H.; Tannenbaum, R. Oxidation of polycrystalline copper thin films at ambient conditions. *J. Phys. Chem. C* **2008**, *112* (4), 1101–1108.

(51) Zhao, B.; Liu, Y.; Zhu, Z.; Guo, H.; Ma, X. Highly selective conversion of CO<sub>2</sub> into ethanol on Cu/ZnO/Al<sub>2</sub>O<sub>3</sub> catalyst with the assistance of plasma. *J. CO<sub>2</sub> Util.* **2018**, *24*, 34–39.

(52) Nixon, K. L.; Pires, W. A. D.; Neves, R. F. C.; Duque, H. V.; Jones, D. B.; Brunger, M. J.; Lopes, M. C. A. Electron impact ionisation and fragmentation of methanol and ethanol. *Int. J. Mass Spectrom.* **2016**, *404*, 48–59.

(53) Wang, G.; Luo, R.; Yang, C.; Song, J.; Xiong, C.; Tian, H.; Zhao, Z.-J.; Mu, R.; Gong, J. Active sites in CO<sub>2</sub> hydrogenation over confined VO<sub>x</sub>-Rh catalysts. *Sci. China Chem.* **2019**, *62*, 1710–1719.

(54) Lou, Y.; Jiang, F.; Zhu, W.; Wang, L.; Yao, T.; Wang, S.; Yang, B.; Yang, B.; Zhu, Y.; Liu, X. CeO<sub>2</sub> supported Pd dimers boosting CO<sub>2</sub> hydrogenation to ethanol. *Appl. Catal., B* **2021**, *291*, No. 120122.

(55) Wang, X.; Ramirez, P. J.; Liao, W.; Rodriguez, J. A.; Liu, P. Cesium-Induced Active Sites for C-C Coupling and Ethanol Synthesis from CO<sub>2</sub> Hydrogenation on Cu/ZnO(0001) Surfaces. *J. Am. Chem. Soc.* **2021**, *143*, 13103–13112.

(56) De Bie, C.; van Dijk, J.; Bogaerts, A. CO<sub>2</sub> Hydrogenation in a Dielectric Barrier Discharge Plasma Revealed. *J. Phys. Chem. C* **2016**, *120*, 25210–25224.

(57) Yang, C.; Mu, R.; Wang, G.; Song, J.; Tian, H.; Zhao, Z.-J.; Gong, J. Hydroxyl-mediated ethanol selectivity of CO<sub>2</sub> hydrogenation. *Chem. Sci.* **2019**, *10*, 3161–3167.

(58) Zhang, S.; Gao, Y.; Sun, H.; Fan, Z.; Shao, T. Dry reforming of methane by microsecond pulsed dielectric barrier discharge plasma: optimizing the reactor structures. *High Volt.* **2022**, *7*, 718–729.

(59) Zhang, S.; Gao, Y.; Sun, H.; Fan, Z.; Shao, T. Charge transfer in plasma assisted dry reforming of methane using a nanosecond pulsed packed-bed reactor discharge. *Plasma Sci. Technol.* **2021**, *23*, No. 064007.

(60) Liu, Z.; Huang, E.; Orozco, I.; Liao, W.; Palomino, R. M.; Rui, N.; Duchon, T.; Nemsak, S.; Grinter, D. C.; Mahapatra, M.; Liu, P.; Rodriguez, J. A.; Senanayake, S. D. Water-promoted interfacial pathways in methane oxidation to methanol on a CeO<sub>2</sub>-Cu<sub>2</sub>O catalyst. *Science* **2020**, *368*, 513–517.